

# Overcoming Water Diffusion Limitations in Hydrogels via Microtubular Graphene Networks for Soft Actuators

Margarethe Hauck, Lena M. Saure, Berit Zeller-Plumhoff, Sören Kaps, Jörg Hammel, Caprice Mohr, Lena Rieck, Ali Shaygan Nia, Xinliang Feng, Nicola M. Pugno, Rainer Adelung,\* and Fabian Schütt\*

Hydrogel-based soft actuators can operate in sensitive environments, bridging the gap of rigid machines interacting with soft matter. However, while stimuli-responsive hydrogels can undergo extreme reversible volume changes of up to  $\approx 90\%$ , water transport in hydrogel actuators is in general limited by their poroelastic behavior. For poly(*N*-isopropylacrylamide) (PNIPAM) the actuation performance is even further compromised by the formation of a dense skin layer. Here it is shown, that incorporating a bioinspired microtube graphene network into a PNIPAM matrix with a total porosity of only 5.4% dramatically enhances actuation dynamics by up to  $\approx 400\%$  and actuation stress by  $\approx 4000\%$  without sacrificing the mechanical stability, overcoming the water transport limitations. The graphene network provides both untethered light-controlled and electrically powered actuation. It is anticipated that the concept provides a versatile platform for enhancing the functionality of soft matter by combining responsive and 2D materials, paving the way toward designing soft intelligent matter.

## 1. Introduction

The field of soft robotics aims to overcome the limitations and drawbacks of rigid and hard machines by fabrication of all necessary components, especially actuators, from soft materials, thereby making human-machine interactions and interfaces safer.<sup>[1,2]</sup> In contrast to stiff parts, soft actuators are able to perform more diverse and complex movements and exhibit greater adaptability.<sup>[3–5]</sup> Prominent materials for soft actuators are smart hydrogels that respond to a stimulus (temperature,<sup>[6]</sup> light,<sup>[7]</sup> pH,<sup>[8]</sup> magnetic<sup>[9]</sup> and electric fields,<sup>[10]</sup> which can lead for example to a deformation of the material. Above all, for application as soft actuator with appropriate work output and power densities<sup>[11,12]</sup> these hydrogels need to provide adjustable and

M. Hauck, L. M. Saure, S. Kaps, C. Mohr, R. Adelung, F. Schütt  
Functional Nanomaterials  
Department of Materials Science  
Kiel University  
24143 Kiel, Germany  
E-mail: ra@tf.uni-kiel.de; fas@tf.uni-kiel.de

B. Zeller-Plumhoff, L. Rieck  
Institute of Metallic Biomaterials  
Helmholtz-Zentrum Hereon  
Max-Planck-Str. 1, 21502 Geesthacht, Germany  
B. Zeller-Plumhoff, R. Adelung, F. Schütt  
Kiel Nano  
Surface and Interface Science KiNSIS  
Kiel University  
24118 Kiel, Germany


J. Hammel  
Institute of Materials Physics  
Helmholtz-Zentrum Hereon  
Max-Planck-Str. 1, 21502 Geesthacht, Germany

A. S. Nia, X. Feng  
Department of Chemistry and Food Chemistry  
Center for Advancing Electronics Dresden (cfaed)  
Technische Universität Dresden  
01062 Dresden, Germany

A. S. Nia, X. Feng  
Max Planck Institute of Microstructure Physics  
Weinberg 2, 06120 Halle, Germany

N. M. Pugno  
Laboratory for Bioinspired  
Bionic  
Nano  
Meta Materials & Mechanics  
Department of Civil  
Environmental and Mechanical Engineering  
University of Trento  
via Mesiano 77, Trento I-38123, Italy

N. M. Pugno  
School of Engineering and Materials Science  
Queen Mary University of London  
Mile End Road, London E1 4NS, UK

 The ORCID identification number(s) for the author(s) of this article can be found under <https://doi.org/10.1002/adma.202302816>

© 2023 The Authors. Advanced Materials published by Wiley-VCH GmbH. This is an open access article under the terms of the Creative Commons Attribution License, which permits use, distribution and reproduction in any medium, provided the original work is properly cited.

DOI: 10.1002/adma.202302816

controllable response times, deformations, actuation stresses, mechanical properties, and cyclic stability. As hydrogels are inherently poroelastic,<sup>[13]</sup> large volumetric deformations over short timescales are limited by the poroelastic time scale of water diffusion.<sup>[14]</sup> One of the most studied smart hydrogels is the thermoresponsive hydrogel poly(*N*-isopropylacrylamide) (PNIPAM)<sup>[6,15,16]</sup> with a lower critical solution temperature (LCST) of about 32 °C.<sup>[17]</sup> Above this temperature, the hydrogel undergoes a reversible phase transition releasing the contained water.<sup>[18,19]</sup> The deswelling results in a volume change that can be used for actuation. However, due to slow response rates (e.g., 12% deswelling within 10 min<sup>[20]</sup>), limiting work output and cycle rate, the properties of bulk PNIPAM hydrogels are not meeting the high requirements needed for soft actuators. In addition to the poroelastic limit, for PNIPAM these limitations are related to the formation of a dense "skin layer"<sup>[21]</sup> during the deswelling process, which greatly reduces the water diffusion out of the hydrogel, requiring weeks to reach equilibrium deswelling.<sup>[22]</sup> Efforts have been made to improve these drawbacks, for example by adding porosity to the hydrogel matrix for an enhanced water transport through the polymer network.<sup>[14,15,23]</sup> However, an increase in porosity to overcome both the poroelastic limit and skin layer effect has a detrimental effect on the mechanical stability of the hydrogel.<sup>[14,24]</sup> In order to combine enhanced water diffusion and enhanced Young's modulus, Alsaid et al. have demonstrated that a highly open porous and interconnected network structure can solve this challenge and achieve remarkable deswelling and swelling rates.<sup>[25]</sup> However, for actuator applications, high actuation stresses and cyclic stability are also required, which are compromised by the introduction of high porosity. Besides the improvement of deswelling and swelling kinetics, providing precise control over the deformation is crucial for the application as soft hydrogel actuator. To achieve accurate actuation, it is essential to have an internal and controllable temperature increase within the hydrogel matrix itself. Photothermal conversion based on light-absorbing filler materials (e.g., carbon-based nanomaterials,<sup>[26,27]</sup> gold nanoparticles<sup>[28,29]</sup> or polymers<sup>[30,31]</sup>) allows untethered<sup>[32,33]</sup> and more flexible operation, but is limited by the area of illumination and depth of light penetration. In contrast, the Joule effect, induced for example by the addition of conductive nanomaterials,<sup>[34]</sup> electrode meshes<sup>[35]</sup> or wires<sup>[36]</sup> to the hydrogel, allows volumetric heating of the hydrogel, but usually compromises its softness.

In this work, we present a bioinspired micro- and nanoengineering concept for hydrogel-based actuators by transferring the ubiquitous motif of hierarchical microtubular networks in nature for efficient fluid transport to hydrogels. Compared to the bulk hydrogel, these structured hydrogels, 1) provide improved actuation dynamics (up to + ≈400%), i.e., improved deswelling and swelling kinetics, 2) perform increased actuation stress (+ ≈4000%), and 3) provide options for controlled actuation by electrical or photothermal heating, all, while maintaining the mechanical stability and the inherently global soft properties of the hydrogel itself. A network of interconnected hollow graphene microtubes with a total porosity of only 5.4% and a very low graphene content of 0.35 vol% is incorporated into a PNIPAM hydrogel matrix. This enhances water transport out of and into the hydrogel matrix for improved actuation dynam-

ics without sacrificing mechanical and cyclic stability, thereby overcoming the general limitation of poroelasticity in hydrogels, as well as PNIPAM specific limitations of skin layer formation associated with bulk PNIPAM hydrogels. For both effects we propose a model for the underlying mechanisms. In addition, the approach allows precise control over the composition of the material system, tailoring properties for different applications, such as untethered, light-driven soft actuators and electrically triggered grippers with control over response times and actuation forces.

## 2. Results

### 2.1. Synthesis of Micro- and Nanoengineered Thermoresponsive poly(*N*-isopropylacrylamide)–Exfoliated Graphene (PNIPAM–EG) Hydrogels

The hierarchical structure of conductive composites of poly(*N*-isopropylacrylamide) (PNIPAM) and exfoliated graphene (EG) as well as their fabrication method, adapted from a previously reported method<sup>[37]</sup> for the fabrication of conductive hydrogels, are shown in **Figure 1a,b**. In short, a sacrificial porous network of interconnected tetrapodal zinc oxide (t-ZnO) (see Figure S1, Supporting Information) is coated with a thin layer of EG by a wet-chemical drop infiltration process, allowing precise control over the EG concentration and layer thickness within the network. Filling of the free volume with PNIPAM and subsequent removal of ZnO by mild wet-chemical etching results in a PNIPAM hydrogel matrix pervaded by interconnected hollow graphene-coated microtubes (see Figure 1a). In the following, this will be referred to as "PNIPAM–EG" (*xx* vol%), (*xx* vol% indicates the graphene concentration) whereas pure, but microstructured PNIPAM, containing a network of hollow microtubes but no EG, will be named PNIPAM-structured, and the bulk PNIPAM will be entitled PNIPAM-bulk. This concept can also be applied to other polymer matrices. By adjusting the density of the sacrificial ZnO template, the overall porosity of the microstructured PNIPAM can be tailored. Here, all samples have a porosity of 5.4%. More complex template geometries can be produced by 3D printing.<sup>[38]</sup> The 3D rendering of segmented pores from microcomputed tomography (microCT) within a region of interest (ROI) of PNIPAM-structured in Figure 1c reveals the interconnected network structure of microstructured PNIPAM hydrogels, displaying the microtube network with an interconnectivity of 70%. This is also shown in a light microscopy image in Figure S2 (Supporting Information). The fabrication method enables the preparation of hydrogel–graphene composites of different shapes and geometries as well as with variable graphene content and patterns (see Figure 1d,e, details in the Experimental Section).

### 2.2. Mechanical Properties and Actuation Performance: Experimental and Modelling

The mechanical properties as well as the deswelling and swelling kinetics of micro- and nanoengineered PNIPAM–EG hydrogels were investigated and compared to pure PNIPAM-structured

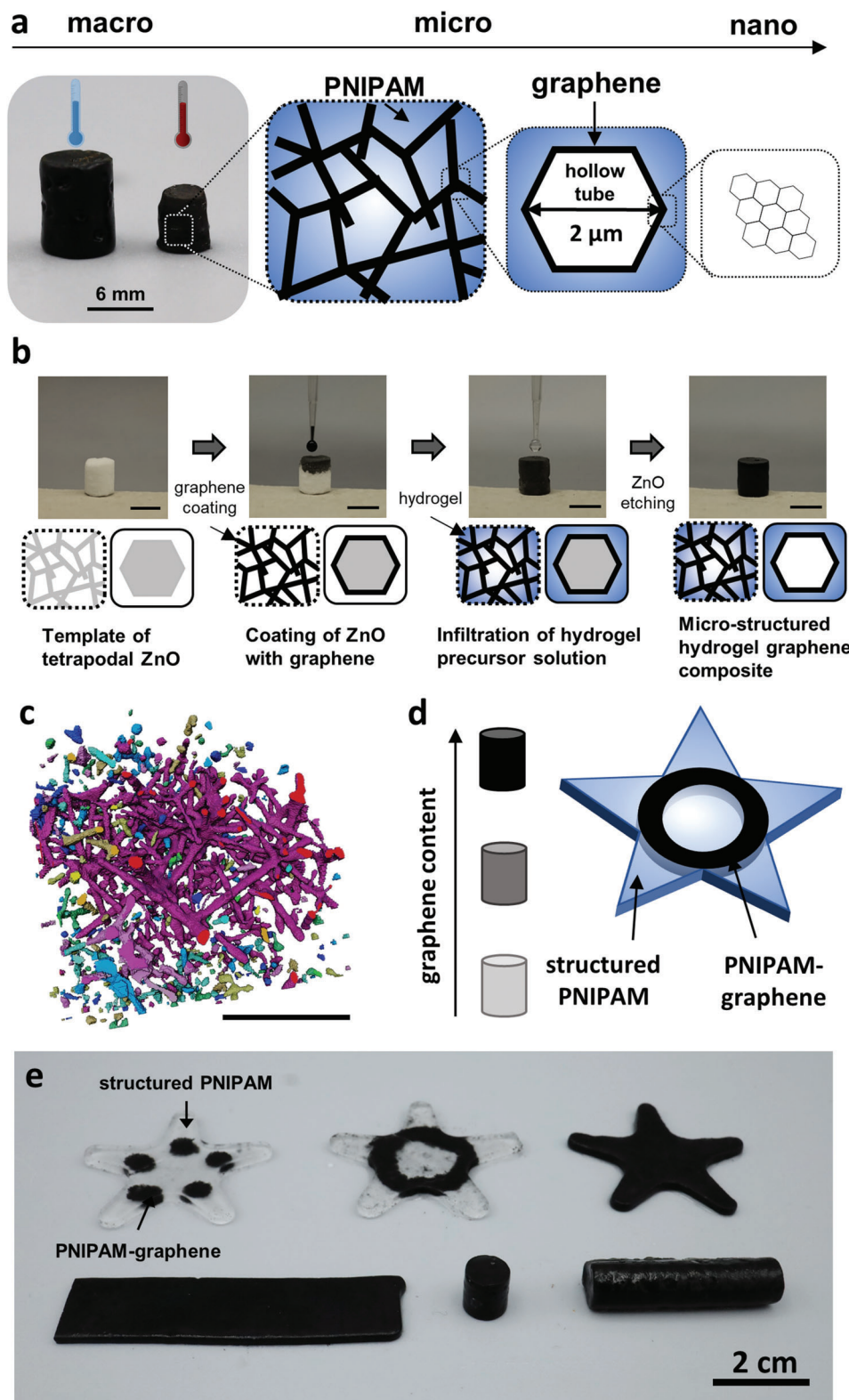


**Figure 1.** Micro- and nanoengineered thermoresponsive poly(*N*-isopropylacrylamide)-exfoliated graphene (PNIPAM-EG) hydrogels. a) Combination of an interconnected hollow graphene microtube network and a PNIPAM hydrogel matrix. b) Fabrication scheme of PNIPAM-EG hydrogels. c) 3D rendering of the microtube network obtained from microcomputed tomography of PNIPAM-structured. Connected components are displayed in the same color. Scale bar: 200  $\mu\text{m}$ . d) The graphene content in PNIPAM-EG hydrogels is adjustable and can be applied to specific regions as a pattern. e) PNIPAM-EG hydrogels with different shapes and geometries as well as with graphene patterns.

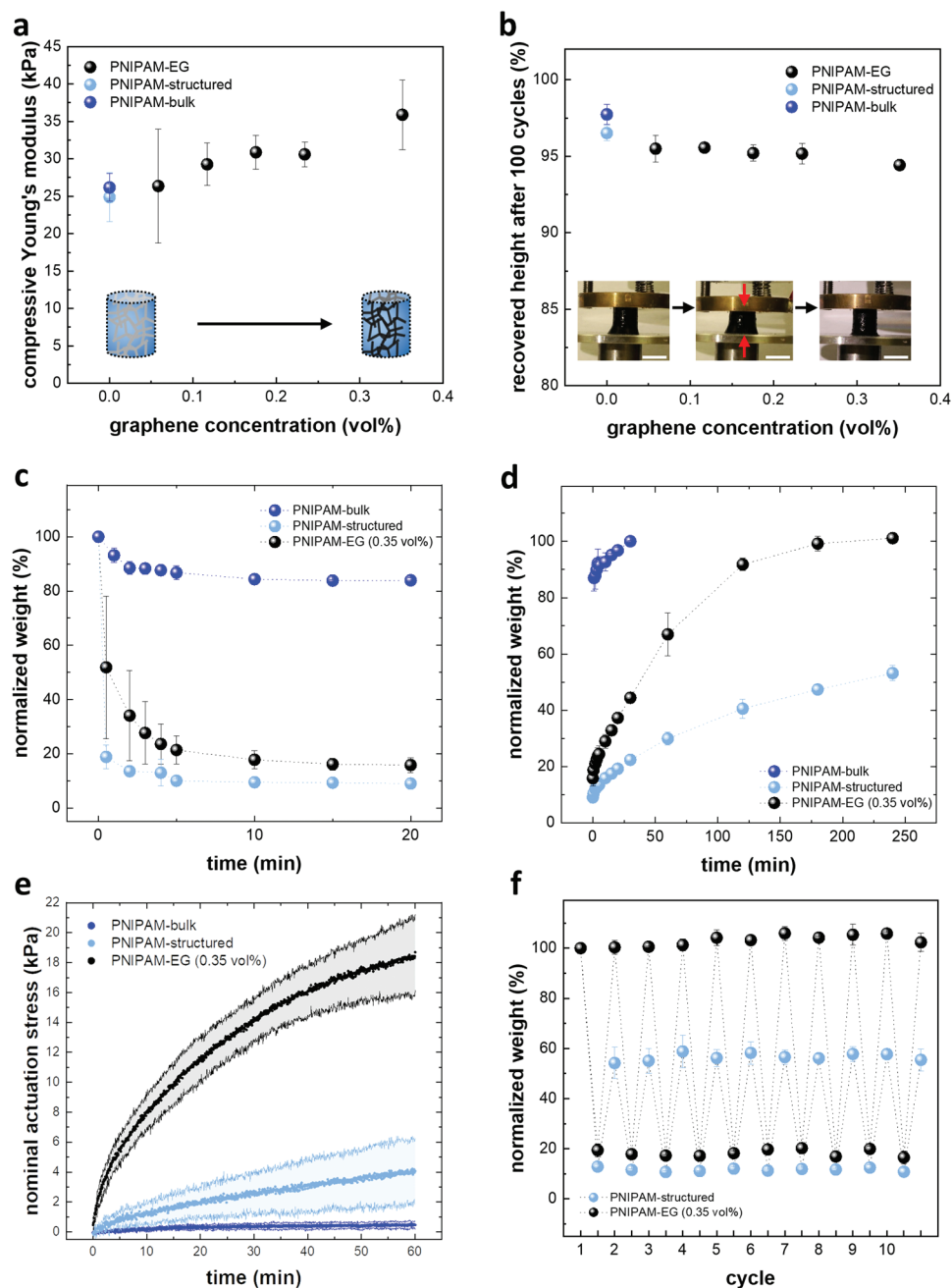


**Figure 2.** Mechanical and actuation properties of micro- and nanoengineered PNIPAM hydrogels in comparison to bulk hydrogels. a) Compressive Young's modulus as a function of graphene concentration, obtained within the initial strain of 5% from the stress–strain curves. b) Cyclic stability in terms of the recovered height after 100 compression cycles at 20% strain. The insets show images of cyclic compression test. Scale bar: 6 mm. c) Deswelling curves and d) swelling curves of PNIPAM-bulk, PNIPAM-structured, and PNIPAM-EG (0.35 vol%). e) Nominal actuation stress performed during swelling of PNIPAM-bulk, PNIPAM-structured, and PNIPAM-EG (0.35 vol%). f) Cyclic deswelling and swelling for 10 cycles of pure PNIPAM-structured and PNIPAM-EG (0.35 vol%). In all graphs, the error bars display the standard deviation ( $n = 3$ ).

and PNIPAM-bulk hydrogels. **Figure 2a** displays the compressive Young's modulus obtained within the initial strain of 5% from the stress–strain curves (see Figure S3, Supporting Information) for PNIPAM-bulk and for microstructured PNIPAM samples with different volumetric graphene concentrations (0 to 0.35 vol%). PNIPAM-bulk has a compressive Young's modulus of 26 kPa. Introducing porosity to the hydrogel system does not

lead to a significant change in Young's modulus. The modulus of 25 kPa determined for PNIPAM-structured agrees with that predicted by a direct rule of mixture (24.6 kPa). Adding 0.35 vol% EG to the hydrogel matrix only increases the compressive Young's modulus to 36 kPa. Applying a direct rule of mixture here again, this suggests an equivalent Young's modulus of the graphene tube of 3.14 MPa (based on experimental data) and a linear

dependence of the compressive Young's modulus with the graphene content, as observed in Figure 2a. Based on the ratio of the relative volumetric contents of pores and graphene in the hydrogel the graphene wall thickness is estimated to be around 32 nm (see Note S1 in Supporting Information for details). The calculations reveal that the incorporation of a graphene network leads to a local stiffening of the microstructured PNIPAM hydrogels but maintains the global soft character, thanks to the hollow nature of the microtubes and low graphene content. The preservation of cyclic stability is demonstrated in Figure 2b, showing that the recovered height after 100 compression cycles at 20% strain ranges between 94.5% and 98% for all sample types. The approach presented here enables the incorporation of an interconnected and continuous microtube network with an overall porosity of only 5.4%, thereby maintaining the mechanical stability. Usually, adding porosity to a hydrogel matrix results in a weakening of material stability.<sup>[24]</sup> Simultaneously, it has been reported previously, that such interconnected microtube networks can strongly enhance the water diffusion compared to bulk PNIPAM hydrogels, improving the deswelling kinetics.<sup>[20]</sup> Figure 2c,d shows the deswelling (at 40 °C) and swelling (at 25 °C) curves as a function of time for PNIPAM-bulk, PNIPAM-structured and PNIPAM-EG (0.35 vol%), respectively. While PNIPAM-bulk only shows a deswelling of 16% within 10 min, PNIPAM-structured deswells by 91% at the same time, demonstrating that incorporation of an interconnected microtube network strongly enhances the water transport compared to bulk PNIPAM hydrogels, as previously reported.<sup>[20]</sup> The deswelling curves indicate that incorporating an additional graphene network in the microstructured hydrogels leads to a slightly reduced total shrinkage (84%) within 10 min, compared to pure PNIPAM-structured. However, while the deswelling behavior is only slightly influenced by the addition of graphene, the swelling behavior (Figure 2d) is drastically improved. While the PNIPAM-EG hydrogels swell to their initial state within 3 h, the pure PNIPAM-structured hydrogels only reach 47% of their initial mass in the same time (see Figure S4, Supporting Information, for photographs of the shrunken and swollen hydrogels). We suspect that this results from two effects:

First, the graphene layer alters the interface of the microtubes between the hydrogel and water-filled channel enhancing the transport through the modified skin layer and through the microtubes (see detailed explanation below). Second, the interconnected graphene network exhibits viscoelastic properties on its own, as shown before.<sup>[39]</sup> Under compressive load the interconnected graphene microtubes buckle at the central tube joints and perform a restoring force upon unloading. We suspect that the restoring force observed for standalone graphene networks also acts in the composite hydrogels, leading to improved swelling kinetics. Indeed, the stress during swelling under the imposed axial confinement is expected to scale as the sum of two contributions: 1) the fluid pressure in the pores generated by capillary stress and 2) the elastic stress generated in the solid phases. The capillary stress  $\sigma_c$  is given by Equation (1):

$$\sigma_c = \frac{2\gamma \cos(\theta)f}{r} \quad (1)$$

where  $\gamma$  is the surface tension of water,  $\theta$  is the contact angle,  $r$  is the channel radius, and  $f$  is the pore volumetric content. The elastic stress  $\sigma_e$  can be calculated according to Equation (2):

$$\sigma_e = \eta E \varepsilon (1 - f) \quad (2)$$

where  $E$  is the Young's modulus of the composite,  $\varepsilon$  is the "potential" strain, and  $\eta$  is an efficiency less than one due to both softening at larger strain and viscoelasticity. The "potential" strain is the one that would be generated in the case of axial confinement removal, and can be estimated by the initial volume ( $V_0$ ) and final volume ( $V$ ) according to Equation (3):

$$\varepsilon = \left(\frac{V}{V_0}\right)^{\frac{1}{3}} - 1 \quad (3)$$

Accordingly, assuming  $\eta = 1$ , the elastic stress would be predicted to be 1.25, 5.60 and 7.68 kPa respectively for PNIPAM-bulk, PNIPAM-structured, and PNIPAM-EG. However, since the capillary contribution for PNIPAM-bulk is expected to be negligible due to the absence of microtubes ( $f = 0$ ), an efficiency  $\eta = 0.37$  is estimated from Equation (2), resulting in an actuation stress of 0.48 kPa as observed experimentally, see Figure 2e (and Figure S5 in Supporting Information for details on the measurement set-up). Assuming the same efficiency for PNIPAM-structured and PNIPAM-EG (with  $f = 0.054$ ), the elastic stresses are calculated to be 2.07 kPa and 2.83 kPa, respectively. The difference of 0.76 kPa suggests that graphene is enhancing the elastic recoil of the still soft hydrogel. Due to the presence of the microtube network in PNIPAM-structured and PNIPAM-EG the capillary contribution to the total actuation stress must be considered. Using Equation (1) to fit the observed total actuation stress of 4.08 kPa for PNIPAM-structured (including the elastic stress of 2.07 kPa), we assume a microtube radius of 1  $\mu\text{m}$  and  $2\gamma\cos(\theta)^{[40]} \approx 37 \text{ mJ m}^{-2}$  is calculated, which is consistent with the reported surface energy of PNIPAM (38.9  $\text{mJ m}^{-2}$ <sup>[41]</sup>). For graphene a value of  $2\gamma\cos(\theta) \approx 60 \text{ mJ m}^{-2}$ <sup>[40]</sup> is reported in the literature. This suggests that graphene is also enhancing the direct solid-water interaction. For PNIPAM-EG, the capillary stress is calculated to be 3.24 kPa and thus a total actuation stress (sum of elastic stress and capillary stress) of 6.07 kPa would be predicted for PNIPAM-EG. This is not in agreement with the experimentally observed total actuation stress, which is 18.7 kPa after 10 min and 21.00 kPa asymptotically (by best fitting with an exponential function (see Figure S6, Supporting Information)), see Figure 2e. To fit the experimental value of 21 kPa, the capillary stress is calculated to be around 18.17 kPa. The difference between estimated (3.24 kPa) and experimental (18.17 kPa) values for the capillary stress suggests the presence of equivalent nanoscopic channels activated by the graphene flakes on the microtube walls. In a simplified calculation according to Equation (1), the mean equivalent radius of the tubes, i.e., the microtubes with superimposed nanoscopic channels, can be estimated to be around  $r = 2\gamma\cos(\theta)f\sigma_c^{-1} \approx 178 \text{ nm}$ , assuming a cylindrical geometry with  $f = 0.054$  and  $\sigma_c = 18.17 \text{ kPa}$ . The presence of these channels is further suggested by the actuation dynamics, as discussed in the next section and is strongly beneficial for improved actuation stress.

Since reversible switching between two states is important for actuation applications, it is demonstrated here with cyclic swelling tests (Figure 2f; photographs in Figure S7, Supporting Information), showing stable deswelling and swelling behavior over 10 cycles for PNIPAM–EG (0.35 vol%) as well as for PNIPAM-structured.

### 2.3. Hypothetical Mechanisms of the Actuation Dynamics

The dynamics of hydrogel actuators are in general governed by water transport processes out of and into the polymeric network, limited by the poroelastic time scale of water diffusion. In the case of PNIPAM, the formation of a skin layer further restricts the actuation dynamics. For a more detailed understanding of the underlying mechanisms, that determine the deswelling and swelling behavior of the three investigated material systems (PNIPAM-bulk, PNIPAM-structured, and PNIPAM–EG), the normalized weight is plotted against  $t^{0.5}$  (Figure 3a), to visualize capillary and diffusion-based processes. For PNIPAM-bulk the deswelling within 20 min is limited to  $\approx 17\%$ , due to a dense skin layer that forms at the outer surface of the sample (Figure S8, Supporting Information), drastically limiting further water diffusion out of the volume (Figure 3b). In contrast, the deswelling of PNIPAM-structured reaches  $\approx 80\%$  within 0.5 min. We suspect that the incorporation of an interconnected microtube network has a combined effect on the limitations due to poroelasticity and skin layer formation (Figure 3c). First, enhanced water transport out of the hydrogel is possible due to the geometrical assembly of the microtube network: 1) the distance between microtubes is small enough to ensure short diffusion pathways of water molecules from the hydrogel matrix to the microtubes, 2) the diameter of the microtubes ( $>2 \mu\text{m}$ ) is large enough for unconfined water diffusion, 3) the microtubes are highly interconnected ( $\approx 70\%$ ). Second, we assume, that upon skin layer formation an increased amount of water is released as more interfacial hydrogel–water area, i.e.,  $188.7 \text{ cm}^2$  compared to  $1.69 \text{ cm}^2$  (factor  $\approx 111$ , calculation details see Note S2, Supporting Information) can be simultaneously dehydrated and transported through the microtubes, explaining the enhanced deswelling characteristics compared to the bulk. We suspect, that the microtubes close during the deswelling process. For PNIPAM–EG a slightly slower initial deswelling can be observed, which can be attributed to a counter force exerted by the interconnected graphene network, still reaching 49% deswelling within 0.5 min. Due to improved solid–water interactions inside the graphene-coated microtubes, we assume that for PNIPAM–EG the microtubes remain partially open and water-filled (Figure 3d), limiting the total deswelling to 84%. With respect to the swelling behavior, PNIPAM-bulk and PNIPAM-structured show an equal slope of  $m_1 = m_2 = 0.029 \text{ s}^{-0.5}$  (Figure 3), which is related to the diffusion coefficient of water during swelling of the PNIPAM polymer network. However, standard methods for determining diffusion coefficients in polymer gels during swelling in a solvent<sup>[42,43]</sup> do not take into account the phase transition in PNIPAM and the associated formation of a skin layer, which requires more complex models in order to provide meaningful results for the diffusion coefficient. The equal slopes indicate that the swelling kinetics are limited by the transport through the dense skin layer and not governed by simple

diffusion through the hydrogel matrix, as otherwise the geometrical factor, i.e., the difference in volume, should lead to different slopes in the  $t^{0.5}$ -plot, due to longer diffusion pathways. Thus, we assume that the water transport through the interfacial skin layer is the rate-limiting process, strongly impairing the swelling of both the bulk and structured hydrogel systems. A completely different behavior is observed for the swelling of PNIPAM–EG hydrogels. Initially, the curve also shows a linear behavior with an increased slope  $m_3 = 0.046 \text{ s}^{-0.5}$  compared to PNIPAM-bulk and PNIPAM-structured. As the volume in the deswollen state of PNIPAM-structured and PNIPAM–EG is comparable, similar slopes are expected. However, as mentioned above, we suspect that the graphene-coated microtubes remain partially open and still contain water in the deswollen state. This shortens the diffusion pathways into the hydrogel volume, leading to an increased slope. At later stages the curve strongly deviates from the linear behavior, which is attributed to different effects. First, the open and water-filled microtubes reduce the water diffusion pathways, resulting in a reduction of the poroelastic diffusion time scale and homogeneous swelling of the PNIPAM–EG hydrogels. Additionally, the incorporation of a graphene network into the hydrogel matrix creates a hydrogel–graphene–water interface inside the microtubes (Figure 3d). We suspect that the altering of the interface influences the water diffusion through the skin layer, resulting in faster swelling kinetics. A possible effect could be that graphene sheets perforate the interfacial skin layer, thereby creating the nanoscopic channels previously discussed and pathways for facilitated water transport through the interface. At the same time, the graphene network performs an increased actuation stress, as shown in Figure 2e, which could also lead to facilitated swelling, as previously quantified.

### 2.4. Photothermal Heating

Next to the improvement of performance characteristics, precise control over trigger options is required for hydrogel-based actuators. While the standard method to induce actuation of thermoresponsive hydrogels is to change the temperature of the surrounding environment, we here show untethered photothermal as well as rapid Joule heating by utilizing the unique properties of graphene, i.e., broadband light absorption and electrical conductivity. Light-induced heating was studied for PNIPAM hydrogels with different graphene concentrations (0.0004–0.18 vol% EG) (Figure 4a). Illumination with white light results in a local light-to-heat conversion in the PNIPAM–EG hydrogel, due to broadband light absorption of graphene, as demonstrated schematically and by thermography in Figure 4b. The maximum surface temperature of the hydrogels is shown in Figure 4c as a function of time for the different graphene concentrations. While the pure PNIPAM-structured only heats up by  $\approx 1 \text{ }^\circ\text{C}$  within 20 s of illumination with  $0.44 \text{ W cm}^{-2}$ , all PNIPAM–EG hydrogels with 0.0021 vol% EG and higher concentrations heat up above the lower critical solution temperature of  $32 \text{ }^\circ\text{C}$  within a few seconds. The initial heating rate (Figure 4d) increases with higher volumetric loadings of EG and reaches values up to  $11.6 \text{ }^\circ\text{C s}^{-1}$  for PNIPAM–EG (0.18 vol%). Figure 4e shows the normalized weight of hydrogels with different graphene concentrations after illumination with  $0.44 \text{ W cm}^{-2}$  for 20 s, highlighting a weight

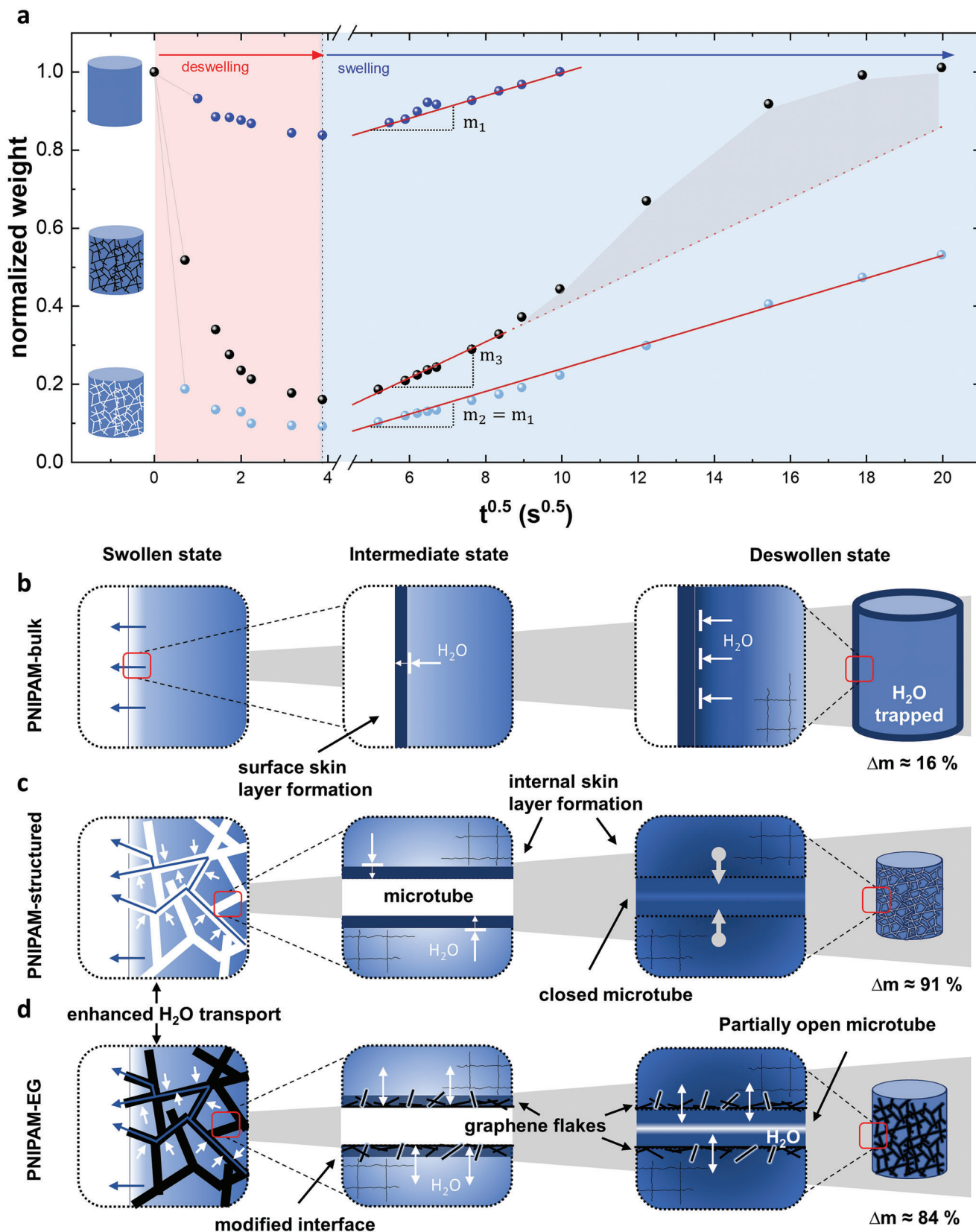


**Figure 3.** Hypothetical mechanisms during the volume change upon phase transition across the LCST of micro- and nanoengineered PNIPAM hydrogels. a) Deswelling and swelling curves as a function of  $t^{0.5}$  of PNIPAM-bulk, PNIPAM-structured and PNIPAM-EG (0.35 vol%). b) The slow and limited

reduction of  $\approx 30\text{--}40\%$  for PNIPAM–EG with 0.0042 vol% and higher concentrations (see Figure S9 in Supporting Information for images of light-induced deswelling). The influence of the illumination time on the deswelling of the hydrogels was measured for PNIPAM–EG (0.06 vol% EG), see inset of Figure 4e, showing that shorter illumination times lead to less deswelling. For low concentrations of EG within the hydrogel matrix, a large fraction of the incoming light is transmitted through the structure, rather than absorbed by the graphene, resulting in a low heating rate of the hydrogel. With increasing EG concentration, more light is absorbed leading to higher temperatures. For the highest measured EG concentration (0.18 vol%), light penetration is limited as light is directly absorbed in the surface region leading to a high surface temperature. However, due to the high water content, heat transport through the hydrogel matrix is limited, resulting in an inhomogeneous deswelling of the sample, see Figure 4e. The increase in temperature upon illumination and thus, the deswelling, can also be controlled by adjusting the light intensity, as demonstrated for PNIPAM–EG (0.06 vol%) in Figure 4f. A light intensity of  $0.44\text{ W cm}^{-2}$  results in fast heating with an initial heating rate of  $9\text{ }^{\circ}\text{C s}^{-1}$ , while a lower intensity of  $0.162\text{ W cm}^{-2}$  leads to an initial heating rate of  $1.5\text{ }^{\circ}\text{C s}^{-1}$ . The findings demonstrate that the temperature increase of PNIPAM–EG can be controlled by varying graphene concentration, light intensity and illumination time, which in turn facilitates control over the deswelling kinetics. Further, photothermal heating is a beneficial tool for any controlled actuation requiring local heating and phase change of the hydrogel, as it is restricted to the area of illumination as the water-containing hydrogel limits the heat transfer throughout the material volume. Figure 4g demonstrates the local heating of a star-shaped PNIPAM–EG hydrogel resulting in the defined movement of only one of the star's arms within 4 s of illumination (see Video S1, Supporting Information).

## 2.5. Joule Heating

In contrast to locally defined heating by photothermal conversion, Joule heating (also referred to as resistive heating) can be used to homogeneously and rapidly heat the entire hydrogel volume in a controlled and defined manner. The interconnected conductive EG network forms pathways of 'microwires' penetrating the entire hydrogel matrix, while the global elasticity of the hydrogel matrix is maintained (see Figure 3a). Previously, it has been demonstrated, that graphene-based aerogels and framework structures provide an excellent platform for the development of innovative energy transducers, e.g., electricity into heat, due to their high conductivity, low density and low volumetric heat capacity.<sup>[44]</sup> Here, we utilize those properties to

rapidly heat our thermoresponsive hydrogel systems to enable a controlled and defined actuation. Most importantly, the establishment of a good electrical contact to the PNIPAM–EG hydrogels is crucial for homogeneous and efficient heating. To ensure that most of the potential drops across the network and is converted into heat, the contact resistance must be lower than the resistance of the graphene network. For this, copper foils and silver wires were attached to both sides of the cylindrical graphene coated ZnO templates using conductive silver paste before filling the template with hydrogel precursor solution during synthesis. Thereby, a specific conductivity of up to  $2.16\text{ S m}^{-1}$  could be obtained for PNIPAM–EG (0.29 vol%). Additionally, the amount of diluted cross-linker solution was increased to 16.1 vol% to reduce the swelling of the hydrogels, and thus, prevent the contact to rupture from the sample during deswelling and swelling. Characterizations of the hydrogels with higher cross-linking can be found in the supplementary information (Figures S10 and S11, Supporting Information), showing the same trends as PNIPAM–EG hydrogels with lower cross-linking. Thermography (Figure 5a) shows that applying a voltage results in a heating of the entire volume of the PNIPAM–EG hydrogels. In turn, the homogeneous heating of the material leads to a uniform deswelling of the entire hydrogel volume, as depicted in Figure 5b for a PNIPAM–EG (0.29 vol%) hydrogel (see Video S2, Supporting Information). By varying the applied voltage, the heating of the material can be controlled, as shown in Figure 5c for a PNIPAM–EG (0.35 vol%) hydrogel, demonstrating that higher applied voltages result in higher heating rates ( $0.6, 1.7,$  and  $2.7\text{ }^{\circ}\text{C s}^{-1}$  for 15, 20, and 25 V, respectively). The resulting length change of the hydrogels also increases with higher applied voltages (Figure 5d), reaching a maximum length change of 22% for a voltage of 25 V. Additionally, Figure S12 (Supporting Information) displays the course of the current of the PNIPAM–EG (0.35 vol%) hydrogel during Joule heating. Homogeneous heating of the hydrogel results in deswelling, and thus, in a compression of the graphene network, bringing the graphene sheets closer together, leading to an increase in current. Further, Joule heating can be performed in a cyclic manner (see Video S2, Supporting Information). The normalized length change for several heating cycles is shown in Figure 5e with an applied voltage of 25 V for 1.5 min and subsequent swelling for 6 min. The length changes by about 17% and almost reaches the initial state after swelling. Again, the current (Figure 5f) increases during electrical heating associated with the compression of the graphene network upon deswelling of the hydrogel.

## 2.6. Actuator Designs

As demonstrated, the precise micro- and nanostructuring of the PNIPAM–EG hydrogels leads to improved actuation dynamics

deswelling of PNIPAM-bulk hydrogels is due to the poroelastic time limit and skin layer formation around the sample which restricts water transport out of the hydrogel. c) Incorporating a network of interconnected microtubes into the hydrogel matrix enhances water transport out of the hydrogel volume, thereby improving the poroelastic limit. At the same time the hydrogel–water interface area is increased by a factor of  $\approx 111$ , enhancing water transport through the skin layer. Both effects result in improved deswelling of PNIPAM-structured hydrogels, while the swelling is still limited, assuming that the microtubes close during deswelling. d) Further coating of the microtubes by graphene additionally modifies the hydrogel–water interface. Thus, the microtubes might remain open and partially water-filled during deswelling which improves the subsequent swelling of PNIPAM–EG hydrogels. Additionally, the graphene flakes might perforate the skin layer, facilitating water transport into the hydrogel volume through nanoscopic channels (as also suggested by modeling), resulting in enhanced swelling.



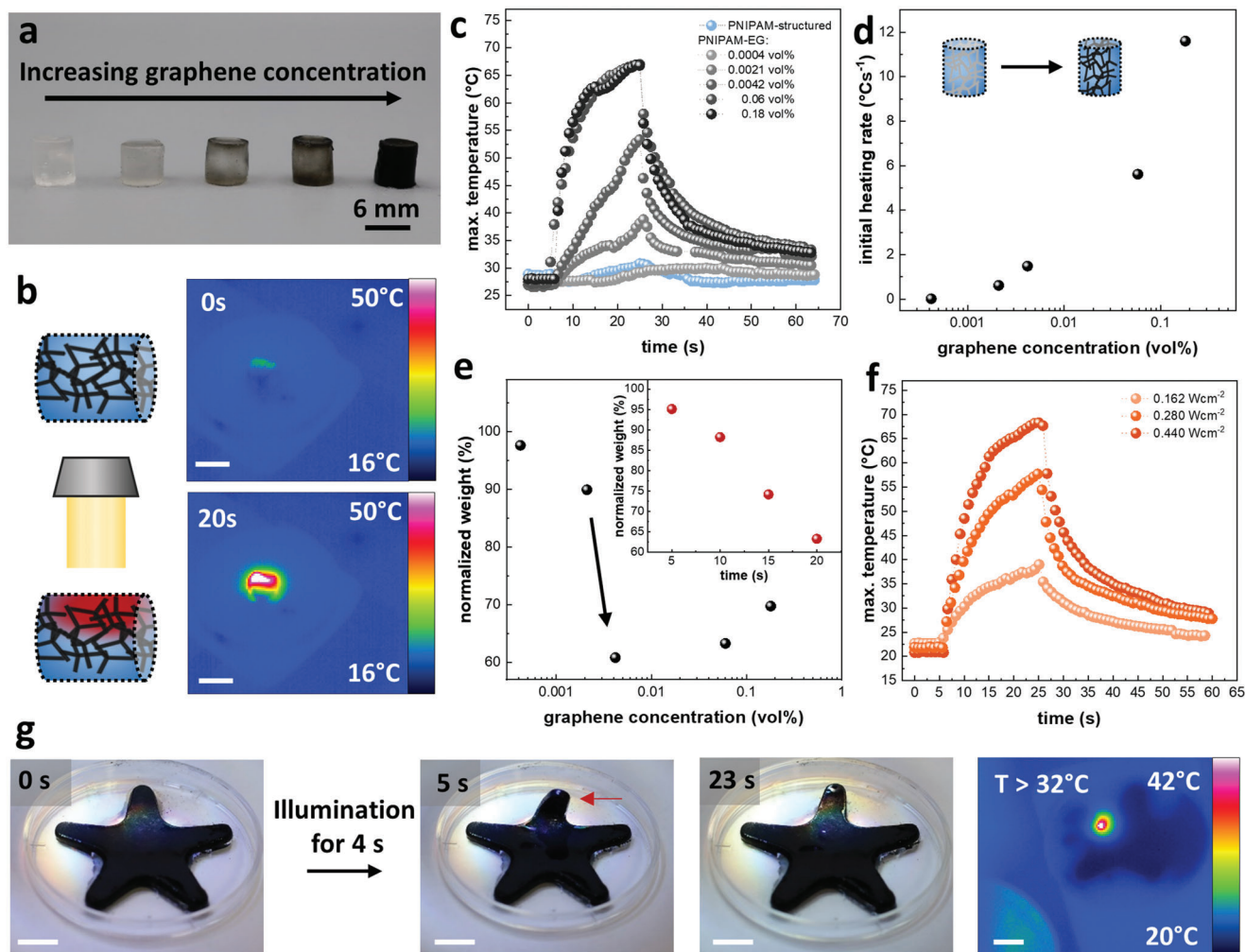


**Figure 4.** Photothermal heating of micro- and nanoengineered PNIPAM–EG hydrogels with varying graphene content. a) Photograph of PNIPAM hydrogels with increasing graphene concentration, from left to right: 0 vol%, 0.0004 vol%, 0.0021 vol%, 0.0042 vol%, and 0.06 vol% EG. b) Schematic representation and thermograms of the photothermal heating of PNIPAM–EG. Scale bar: 6 mm. c) Temperature curves of PNIPAM hydrogels with varying EG content, upon illumination with white light ( $0.44 \text{ W cm}^{-2}$ ) and d) corresponding initial heating rate as a function of graphene concentration. e) Normalized weight as a function of graphene concentration after illumination with white light ( $0.44 \text{ W cm}^{-2}$ ) for 20 s. The inset shows the normalized weight as a function of illumination time for PNIPAM–EG (0.06 vol%). f) Temperature curves of PNIPAM–EG (0.06 vol%) for different light intensities. g) Photographs and corresponding thermogram of a star-shaped PNIPAM–EG hydrogel, locally illuminated for 4 s with white light ( $0.44 \text{ W cm}^{-2}$ ). Scale bar: 5 mm.

and performance, while also enabling internal heating of the hydrogels. To demonstrate the suitability and variability of the microengineered hydrogels for soft actuators, different actuator designs and concepts were developed and studied. For an untethered, light-controlled actuation a beam actuator and a bilayer-structured gripper were designed. The beam actuator (Figure 6a) can be actuated by local heating with light, leading to a local temperature increase above the LCST within 20 s (Figure 6b). Local deswelling then results in a lift of the attached weight, as demonstrated in Figure 6c for two different weights. The motion can be performed in cyclic manner in water ( $T < \text{LCST}$ ), as shown in Video S3 (Supporting Information) and Figure 6d, displaying the height of the lifted weight (1 g). Further, the presented microstructuring approach facilitates the fabrication of a bilayer-structured gripper for untethered, light-controlled actuation.

The gripper consists of a microstructured PNIPAM–EG layer and an unstructured PNIPAM layer on top (Figure 6e). The two layers consist of the same hydrogel (PNIPAM). Thus, the bilayer structure can be prepared by filling the t-ZnO–EG template, used for microstructuring, with the hydrogel precursor solution and pouring excess solution onto the template to create the additional unstructured PNIPAM layer. In contrast to other approaches,<sup>[45–48]</sup> here only one hydrogel system and polymerization step is needed without any further chemical modification. The introduction of strain in the bilayer structure results from two effects: first, the PNIPAM–EG layer heats up upon illumination, unlike the pure PNIPAM layer, and second, the microstructured PNIPAM–EG layer additionally shows a stronger deswelling than the unstructured PNIPAM layer. The gripper can be actuated by global illumination, leading to heating and strong

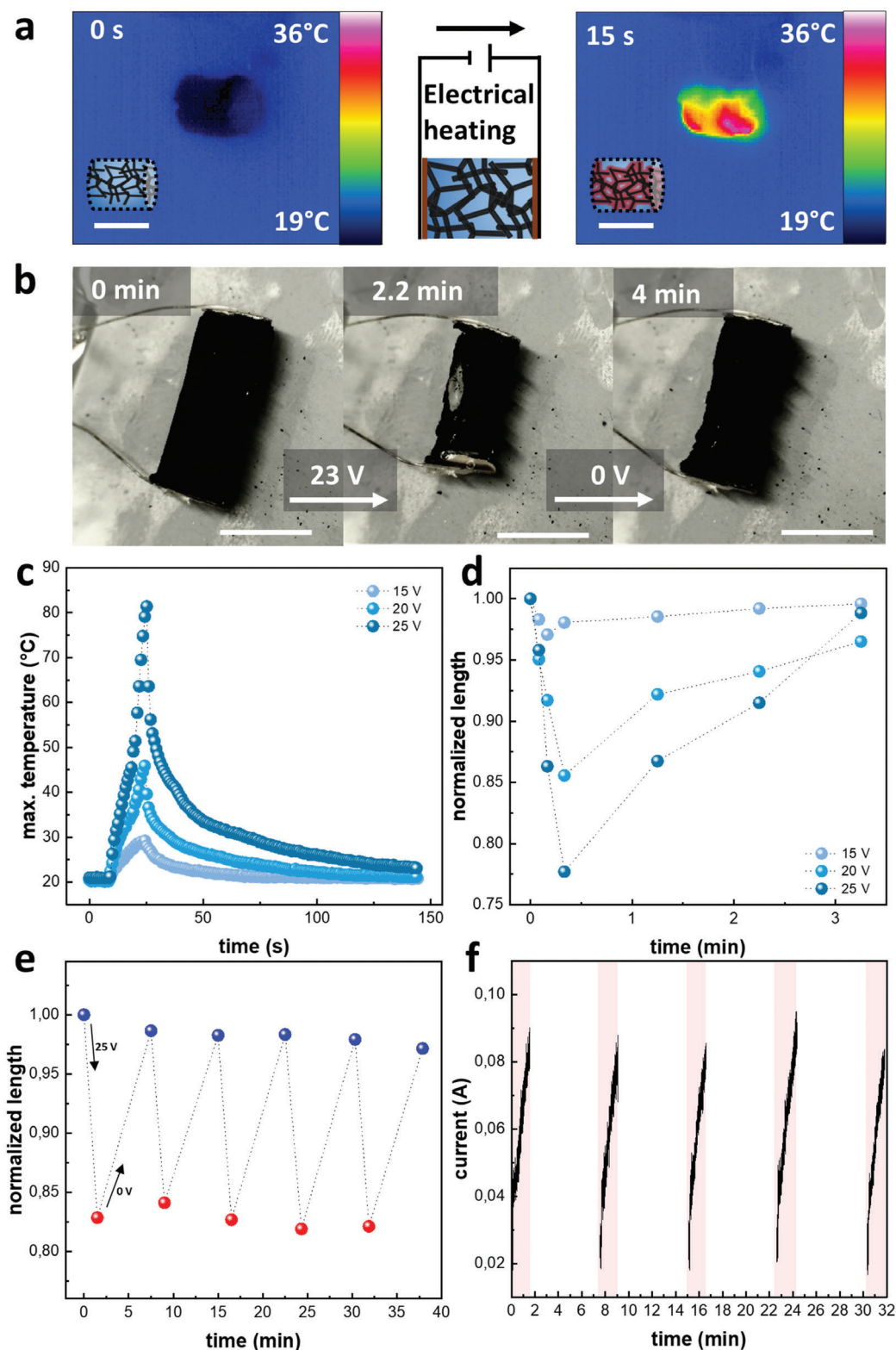
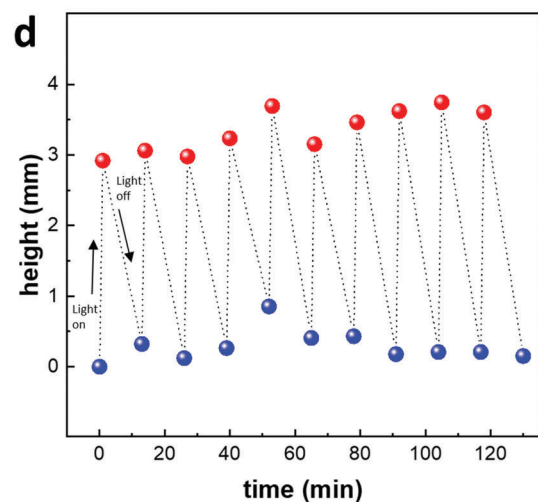
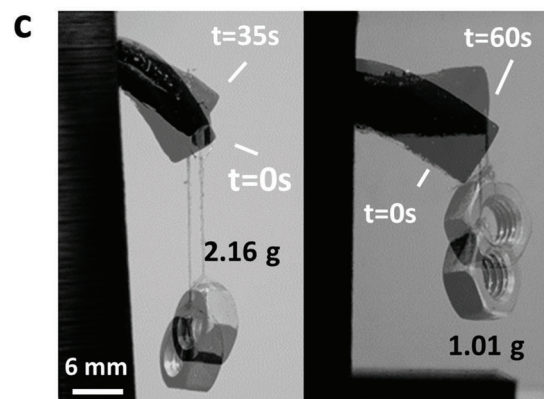
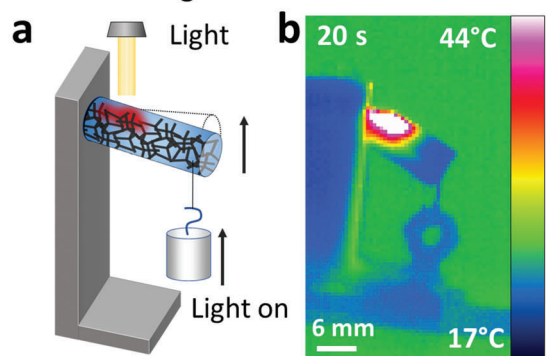
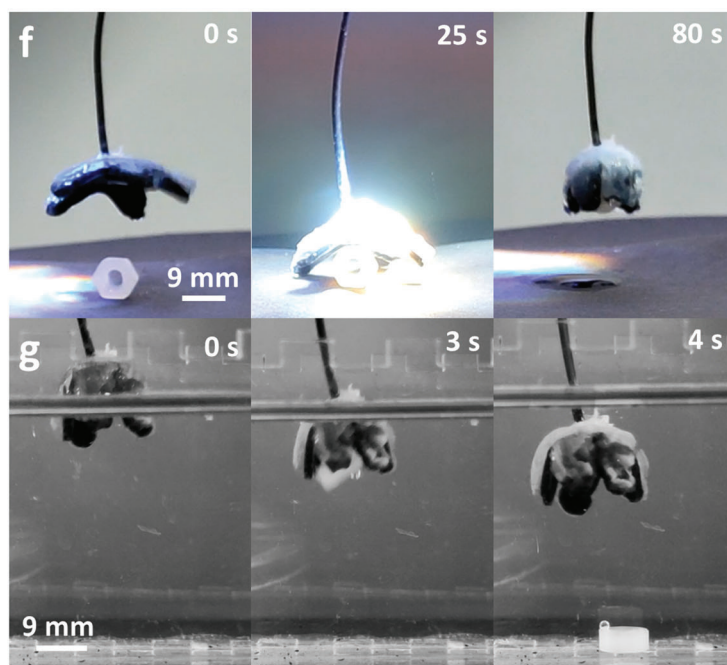
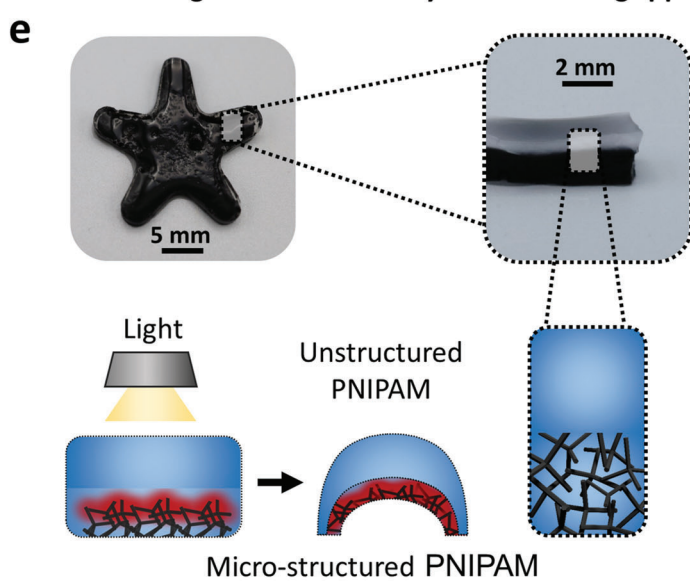


**Figure 5.** Volumetric Joule heating of micro- and nanoengineered PNIPAM-EG hydrogels. a) Thermograms of electrically heated PNIPAM-EG hydrogel. Scale bar: 6 mm. b) Photographs of PNIPAM-EG (0.29 vol%) hydrogel heated with 23 V in water. Scale bar: 6 mm. c) Temperature curves and d) corresponding normalized length as a function of time for different applied voltages for a cylindrical PNIPAM-EG (0.35 vol%) sample with 6 mm height. e) Cyclic deswelling and swelling of an electrically heated PNIPAM-EG (0.35 vol%) hydrogel (10 mm height) in water, in terms of the normalized length as a function of time and f) corresponding current curves.

**Untethered light-controlled beam actuator**



**Untethered light-controlled bilayer-structured gripper**



**Electrically powered gripper by volumetric heating**

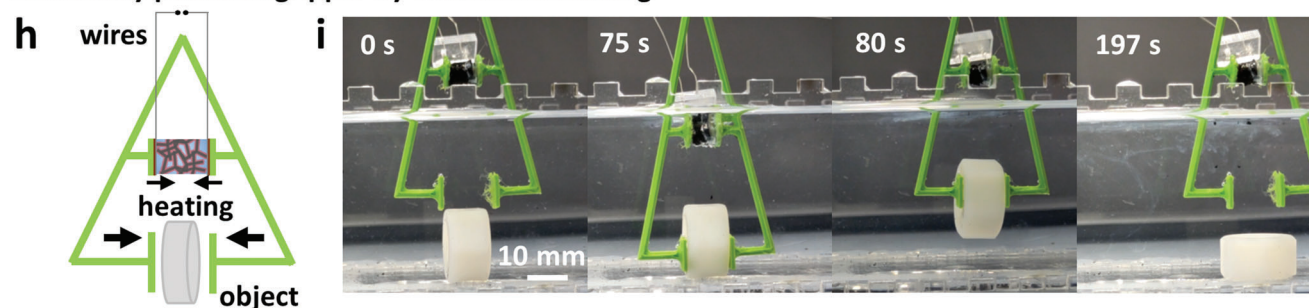


**Figure 6.** Hydrogel actuator designs and concepts based on micro- and nanoengineered PNIPAM-EG hydrogels. a) Schematic of concept for an untethered light-controlled beam actuator. b) Thermogram of beam actuator, illuminated with white light ( $0.44 \text{ W cm}^{-2}$ ). c) Merged photographs of beam

deswelling of the microstructured PNIPAM–EG layer, whereas the unstructured PNIPAM layer deswells only slightly, resulting in a strain and final grasping of an object within 80 s, shown in Figure 6f and Video S3 (Supporting Information). The object can be released instantly by placing the gripper in water ( $T < LCST$ ) (Figure 6g). Reusability is proven in Figure S13 (Supporting Information) by cyclic actuation. To demonstrate the application of volumetric Joule heating an electrically powered gripper was designed (Figure 6h). The actuation is shown in the image series in Figure 6i and Video S3 (Supporting Information). Joule heating with 25 V results in deswelling of the PNIPAM–EG hydrogel and the gripper closes via force transmission and thus, an object can be moved. Upon cooling and swelling of the hydrogel in water, the gripper opens again and the object is released.

### 3. Discussion

As demonstrated, the incorporation of highly interconnected microtubular graphene networks into PNIPAM hydrogels results in improved actuation dynamics and stresses compared to bulk hydrogels, while maintaining global elasticity and mechanical stability of the hydrogel matrix. For comparison with previous advances and achievements of PNIPAM-based hydrogels and hydrogel actuators, representative studies are listed in **Table 1**, comparing key performance metrics for soft actuators, previously proposed by Li et al.<sup>[11]</sup> While many studies provide some characterization of the deswelling and swelling kinetics and demonstrate some actuator designs, almost no study provides values for the actuation stress, actuation strain as well as power and work densities, which are essential for evaluation and comparison of the performance of soft actuators. Furthermore, a direct comparison between these individual studies is not meaningful, as sample geometries differ strongly. For example, several studies have investigated the deswelling and swelling kinetics of PNIPAM-based hydrogels in the form of thin layers, demonstrating remarkably fast switching between the two states, as the water diffusion pathways are rather small in these thin layers compared to hydrogel actuators with larger volumetric dimensions, such as those demonstrated in this work. In addition, while thin layers provide fast actuation dynamics their nominal actuation stress is rather low, which limits their application in soft robotics. To enhance the actuation dynamics of volumetric thermoresponsive hydrogels, the introduction of high porosities into the hydrogel matrix can significantly improve the actuation kinetics<sup>[25]</sup> by improving water transport. However, a high porosity simultaneously weakens the internal cohesion of the material, leading to a loss in load-bearing capacity and compromises the mechanical integrity and stability of the hydrogel. As a result, the maximum actuation stress is reduced. In contrast, in our work, we added only a marginal fraction of 5.4% porosity to the hydrogel matrix, thereby maintaining its mechanical stability. To facilitate the comparison of hydrogel-based actuators in future studies, standardized test methods need to be established to make useful comparisons of

material and actuation properties to identify advances. With respect to the key performance metrics discussed above, this work addresses all challenges relevant to hydrogel actuators by combination of enhanced actuation dynamics and stresses, cyclic mechanical stability and trigger options.

### 4. Conclusion

We have presented a micro- and nanoengineering approach for the preparation of thermoresponsive hydrogel-based soft actuators with improved actuation stress and dynamics and overall performance. Incorporation of an interconnected microtube graphene network into a PNIPAM matrix overcomes the limitations related to poroelasticity and skin layer formation in bulk PNIPAM hydrogels. This leads to an improvement in actuation dynamics of up to  $\approx 400\%$ , while the introduction of only 5.4% porosity maintains mechanical stability. The combination of interconnected graphene network and hydrogel matrix results in increased actuation stress ( $+ \approx 4000\%$ ), without compromising the global softness of the PNIPAM matrix. Tailoring the graphene concentration within the material system provides easy control over response times and enables the application in soft actuation systems. Besides the standard actuation method for thermoresponsive hydrogels, the presented PNIPAM–EG hydrogel system allows untethered, light-triggered as well as electrically powered and controlled actuation for soft actuators. The concept is transferable to other hydrogel systems to overcome poroelastic limitations, while allowing the incorporation of microtube networks composed of other nanomaterials, thereby extending their functionalities for application as soft sensors and actuators.

### 5. Experimental Section

*Fabrication of Microstructured Hydrogels:* Microstructured poly(*N*-isopropylacrylamide) (PNIPAM) hydrogels were prepared by using sacrificial templates from tetrapodal zinc oxide (t-ZnO). t-ZnO powder was prepared by a flame transport synthesis, described in detail elsewhere.<sup>[54,55]</sup> The loose t-ZnO microparticles were pressed into templates using metal molds with desired geometry (cylindrical ( $d = 6$  mm,  $h = 6/10/13/20$  mm) or star-shaped ( $h = 2$  mm)). In this work, sacrificial templates with  $0.3$  g cm<sup>-3</sup> t-ZnO were prepared and then sintered at  $1150$  °C for  $5$  h to obtain stable, interconnected networks. The desired density was achieved by using the appropriate amount of t-ZnO for a given volume of the mold. For the preparation of microstructured conductive poly(*N*-isopropylacrylamide)–exfoliated graphene (PNIPAM–EG) hydrogels, the ZnO tetrapods were coated with a thin layer of graphene by a wet-chemical infiltration method, reported in a previous publication.<sup>[39]</sup> For this, the entire free volume of the t-ZnO templates was filled with an aqueous dispersion of electrochemically exfoliated graphene (EG) ( $1.4$  mg mL<sup>-1</sup>) and dried on a heating plate at  $40$  °C for  $4$  h, resulting in a homogeneous coating of the ZnO tetrapod arms. PNIPAM–EG hydrogels with different graphene concentrations, ranging from  $0.0004$  to  $0.35$  vol%, were prepared by either diluting the EG dispersion or performing multiple infiltration steps. Samples intended for Joule-heating were then contacted using silver paste (Acheson 1415) and copper foil. To obtain patterned

actuator, lifting attached weights. d) Height of the attached weight as a function of time for multiple actuation cycles of the beam actuator in water. e) Photographs and schematic of an untethered light-controlled gripper, consisting of a microstructured PNIPAM–EG layer with an unstructured PNIPAM layer on top. f,g) Photo series of grasping (f) and releasing (g) an object by the light-controlled gripper. h) Schematic of an electrically powered gripper by volumetric Joule heating. i) Photo series of grasping and releasing an object by the electrically powered gripper.

**Table 1.** Comparison of representative studies on PNIPAM-based hydrogels and actuators. (*h*: height, *L*: length, *d*: diameter, *V*: volume, *m*: mass, *E*: elastic modulus, *G*: storage modulus).

Material system	Material properties				Actuator properties					Ref.
	Deswelling	Swelling	Mechanics	Actuation Strain and Stress	Actuator designs	Trigger options	Work density ( $\text{J m}^{-3}$ )	Power density ( $\text{W m}^{-3}$ )	Cycle performance (cycles)	
PNIPAM-structured	$\Delta m/m = 0.6h$ = 0.6(5.4% porosity)	$\approx 24$ h	Compressive $E = 25$ kPa; 98% recovered height after 100 compression cycles at 20% strain	$\approx 50\%$ >4.08 kPa	Beam with bending motion; Light-driven bilayer gripper per/electrically driven gripper	Light, Joule heating ( $2.16 \text{ S m}^{-1}$ )	95.6 (for weight lifting beam)	3.2 (for weight lifting beam)	> 10	This work
PNIPAM-exfoliated graphene	$\Delta m/m = 0.6h$ = 0.6(5.4% porosity)	$\approx 10.800$	Compressive $E = 36$ kPa; 95% recovered height after 100 compression cycles at 20% strain	$\approx 50\%$ >18.7 kPa	Beam with bending motion; Light-driven bilayer gripper per/electrically driven gripper	Light, Joule heating ( $2.16 \text{ S m}^{-1}$ )	95.6 (for weight lifting beam)	3.2 (for weight lifting beam)	> 10	This work
PNIPAM-alginate-carbon nanofibers	$\Delta V/V = 67.5\%$ @ 60 s	–	$\approx 3$ MPa compressive strength; 83% strain at failure; $E = 17$ MPa	20% (for actuation by Joule heating)	–	Joule heating ( $66 \text{ mS cm}^{-1}$ )	–	–	–	[34]
Nanostructured PNIPAM	Cylinder $d = 1.5h$ = 0.3	–	Compressive $E = 2.64$ kPa	–	–	–	–	–	–	[53]
Porous PNIPAM-alginate	Cylinder $d = 1.5h$ = 0.9	–	Compressive $E = 17$ kPa; $G = 4.4$ kPa	–	–	–	–	–	–	[52]
Nanostructured PNIPAM	Disc $d = 2.2h$ = 0.9	–	Up to 1700 kPa tensile strength; Up to 1710% elongation ratio at break; $E \approx 1$ kPa to $\approx 23$ kPa	–	–	–	–	–	–	[23]

(Continued)

**Table 1.** (Continued).

Linear actuators and grippers without characterized bending motion										
Material system	Material properties				Actuator properties					Ref.
	Geometry (cm)	Deswelling	Swelling	Mechanics	Actuation Strain and Stress	Trigger options	Work density ( $\text{J m}^{-3}$ )	Power density ( $\text{W m}^{-3}$ )	Cycle performance (cycles)	
PNIPAM-graphene oxide	Discs $\approx 1.3h = 0.5$	$\Delta V/V = >85\%$ in 600 s	$\approx 24$ h	Up to 700 kPa tensile strength; up to 28000% fracture strain; $E \approx 8$ kPa to $\approx 46$ kPa	–	Remote controlled switch	–	–	$>4$	[27]
Hierarchically open porous PNIPAM	Square $1.4 \times 1.4 \times 3$	$\Delta V/V = 60\%$ @ 35 s	$\approx 70$	Compressive $E \approx 40$ kPa; withstands 500 g weight;	–	Blooming flowers	–	–	–	[25]
PNIPAM with embedded thin flexible electrode mesh	Square $1.5 \times 0.8 \times 0.1$	$\Delta L/L = 35\%$ @ 45 s	$\approx 480$	–	35%	Combination of hydrogel and heater meshes for programmable shape in 2D and 3D	–	–	$>2$	[35]
Linear actuators and grippers with characterized bending motion										
PNIPAM-poly pyrrole	Square $1 \times 1 \times 0.4$	$\Delta V/V = 70\%$ @ 480 s	–	30 kPa tensile strength; 210% fracture strain	–	Locomotion; sensing; signal-tracking; bending; weight-lifting; object grasping; transporting	–	–	$>5$ for bending	[30]
PNIPAM-carbon nanotubes; packaged in polyvinylidene chloride film	Rectangle $2.2 \times 2 \times 0.1$ (between 0.75 to 2) $\times 0.1$	–	$\approx 720$ (for bending)	–	$\approx 210^\circ$ @ 72 s $\approx 42$ mN	Bending; using body heat as wearable device; sunlight-operated curtain	–	–	$>10$	[49]

(Continued)

**Table 1.** (Continued).

Material system	Material properties				Actuator properties				Ref.		
	Deswelling		Swelling	Mechanics	Actuation Strain and Stress	Actuator designs	Trigger options	Work density ( $\text{J m}^{-3}$ )		Power density ( $\text{W m}^{-3}$ )	Cycle performance (cycles)
	Geometry (cm)	Kinetics	Kinetics (Recovery time in s)								
PNIPAM-reduced graphene oxide	Square thickness > 140 $\mu\text{m}$	$\Delta V/V = 80\%$ @ 180 s (by irradiation)	900	–	Full bending motion @ 30 s	Bilayer actuator with polyacrylamide as passive layer; bending	Light	–	–	–	[50]
PNIPAM sponge	Square $2 \times 2 \times 0.1(92\%$ porosity)	$\Delta V/V = 60\%$ @ 7 s	7	50 kPa tensile strength; 85% fracture strain	$\approx 400^\circ$ @ 10 s	Bilayer actuator with paper as passive layer; bending; grasping; bilayer actuator with $\text{Fe}_3\text{O}_4$ for locomotion	Bilayer with PNIPAM/PNIPAM- $\text{Fe}_3\text{O}_4$ for actuation by NIR light	–	–	> 5 for PNIPAM sponge	[51]
PNIPAM-Al-/Na-alginate	Geometry not provided	650 wt% water loss @ 300 s	600 (for bending)	Withstands 6.3 MPa compressive stress at 95% strain; 322 kPa tensile strength; $E = 185 \text{ kPa}$ ; $\approx 9$ of uniaxial stretch	$140^\circ$ @ 40 s	Bilayer beam actuator with bending motion; Gripper (max. load 1.21 g)	–	–	–	> 3 for bending	[48]
Gradient-porous PNIPAM	Disc $d = 9 \text{ h}$ not provided	$d/d_0 \approx 80\%$ @ 35 s	35	Compressive $E = 7.5 \text{ kPa}$ ; withstands 90% compression	$70^\circ$ @ 5 s	Locomotion; bending; twisting; curving; octopus-like swimming; weight lifting;	NIR light (by incorporation of polypyrrole)	763 (calc. based on weight lifting)	42.4 (calc. based on weight lifting)	> 5	[31]

samples, EG dispersion was dribbled only on strongly localized areas of the ZnO template, not filling the entire free volume of the sample. Subsequently, a precursor solution of the hydrogel (PNIPAM) was prepared by mixing ammonium persulfate (APS) (1:10 solution, 100  $\mu\text{L}$ ), distilled water (dH<sub>2</sub>O) (1000 or 750  $\mu\text{L}$ ), 2%-*N,N'*-methylenebisacrylamide (BIS) (500 or 750  $\mu\text{L}$ ), 20%-*N*-isopropylacrylamide (NIPAM) (3000  $\mu\text{L}$ ) and *N,N,N',N'*-tetramethylethylenediamine (TEMED) (46  $\mu\text{L}$ ) (all chemicals purchased from Sigma Aldrich) in a beaker and infiltrated into the templates to fill up the entire free volume. Bulk hydrogels were prepared by pouring the solution into cylindrical molds with diameter and height of 6 mm. Bilayer-structured samples were prepared by placing a star-shaped ZnO template in a well plate and filling the well with an additional layer ( $\approx 2$  mm) of hydrogel precursor solution. All samples were prepared with 10.8 vol% diluted cross-linker solution (2%-BIS) except samples for Joule heating which were fabricated with 16.1 vol% diluted cross-linker solution. After 5 h of polymerization the samples were either placed in distilled water (bulk samples) or in diluted hydrochloric acid (HCL, 0.5 M) for 3 days to etch the t-ZnO resulting in microstructured samples with an overall porosity of 5.4%. The porosity was calculated from the volume occupied by t-ZnO  $V_{\text{t-ZnO}}$  and the volume of the template  $V_{\text{template}}$  according to Equation (4):

$$\text{Porosity (\%)} = \frac{V_{\text{t-ZnO}}}{V_{\text{template}}} \quad (4)$$

Afterward, all samples were thoroughly washed with distilled water by exchanging the water twice a day for at least 5 days to remove access monomers and acid.

**Micro Computed Tomography:** For micro computed tomography (microCT) analysis a PNIPAM sample was cut to a size of  $\approx 1.6 \times 1.6 \times 3.75$  mm<sup>3</sup> and secured by mounting on a 0.2 mm diameter drill. The sample was then placed in a Kapton tube of 1.6 mm diameter with water to ensure its hydration. Both ends of the Kapton tube were sealed using radio-transparent resin hardened using blue light (easyform LC, DETAX GmbH & Co. KG, Ettlingen, Germany). The sample was at the P05 microtomography beamline IBL operated by Helmholtz-Zentrum Hereon at the PETRA III storage ring at Deutsches Elektronen-Synchrotron (DESY) in Hamburg. The photon energy was set to 30 keV. A 5120  $\times$  3840 pixel KIT CMOS camera was used at 10 $\times$  magnification, resulting in an effective pixel size of 0.64  $\mu\text{m}$ . To achieve sufficient propagation-based phase contrast, the sample-to-detector distance was set to 500 mm. The sample movement was minimized further by performing a flyscan with 2000 projections (with 20 dark and 300 flat field images) and an exposure time of 200 ms, thus leading to an overall scan time of  $\approx 4$  min. The tomogram reconstructed with bin 2 using a customized reconstruction tool<sup>[56]</sup> that uses the Astra Toolbox<sup>[57,58]</sup> in Matlab R2021b (The MathWorks Inc., USA).

Due to high image noise from fast imaging and ring artifacts, the image was filtered using a custom filter to remove ring artifacts implemented in Python (Anaconda 3, version 5.2), followed by iterative non-local means filter<sup>[59]</sup> with an isotropic search radius of 6 voxel and 4 iterations. As some sample regions displayed minor movement and remaining artifacts, a region-of-interest (ROI) of  $0.355 \times 0.355 \times 0.357$  mm<sup>3</sup> was selected for analysis. The trainable WEKA plugin<sup>[60]</sup> in Fiji/ImageJ<sup>[61]</sup> was used for the segmentation of the pores. The connectivity of the sample was determined in Avizo 2021.1 (FEI SAS, Thermo Scientific, France) allowing for a minimum component size of 27 voxels and corner connectivity. Finally, the connectivity was calculated as the fraction of the volume of the largest connected pore divided by the overall pore volume.

**Deswelling and Swelling Tests:** Deswelling and swelling curves were recorded by storing the cylindrical samples ( $d = 6$  mm,  $h = 6$  mm) in a water bath at 40 or 25  $^{\circ}\text{C}$ , respectively, and weighing the samples at distinct time points. For cyclic tests, the samples were weighed after 15 min in a water bath at 40  $^{\circ}\text{C}$ . Subsequently, the samples were kept in a water bath at 25  $^{\circ}\text{C}$  for 3 h and then weighed. Triplicates were measured.

**Cyclic Compression Tests:** The cyclic compression tests of swollen cylindrical samples ( $d = 6$  mm,  $h = 6$  mm) were performed using a customized set-up (Märzhäuser Wetzlar HS 6.3 micromanipulator and force sensor (burster, type 9235/36)), controlled by a LabView program. Compression

tests were performed in air at a strain rate of 2% s<sup>-1</sup>. Triplicates were measured.

**Measurement of Nominal Actuation Stress:** The measurement of the nominal actuation stress during swelling was conducted with the same setup as for the cyclic compression tests. First, the cylindrical samples ( $d = 6$  mm,  $h = 6$  mm) were dehydrated in a water bath at 40  $^{\circ}\text{C}$  and then placed between the upper and lower plate in a water bath at 25  $^{\circ}\text{C}$ . The plates stayed at a constant position while the exerted force was measured.

**Light- and Electrically Induced Heating:** The light-induced heating was characterized with a self-built set-up consisting of a beamer (Acer, DLP Projector, DNX0906) and a Fresnel lens (from an overhead projector) to focus the light onto the sample. The light intensity was controlled using a powerpoint presentation with different grey scales and measured by a photometer (Thorlabs Photometer, S425C-L with Interface PM100USB and Thorlabs Optical Power Monitor). For the determination of light-induced deswelling, the samples were weighed before and after illumination. Characterization of light-induced heating was performed in air with cylindrical samples ( $d = 6$  mm,  $h = 6$  mm).

For Joule heating, silver wires were attached to the copper foil at both sides of the PNIPAM-EG hydrogels using conductive silver paste (Acheson 1415). A constant voltage was applied using a USB-2537 High-Speed DAQ Board (Measurement Computing Corporation, USA) and a self-written LabView program with an EA-PS 2042-10B (EA Elektro-Automatik, Germany) as power supply. Simultaneously, voltage and current were measured as a function of time. Characterization of the temperature profiles and respective deswelling were performed in air with cylindrical samples ( $d = 6$  mm,  $h = 6$  mm), while cyclic tests were performed in distilled water with cylindrical samples with a height of 10 mm or 13 mm. The specific conductivity  $\sigma$  was calculated from the current  $I$ , the voltage  $U$ , sample length  $l$  and sample cross-section  $A$  according to Equation (5):

$$\sigma = \frac{l \times I}{U \times A} \quad (5)$$

Temperature recording was done with an IR-thermo camera (IRBIS) in combination with IRBIS professional software.

**Actuator Designs:** For the beam actuator a cylindrical PNIPAM-EG (0.18 vol% EG, 10.8 vol% diluted cross-linker solution) hydrogel with 2 cm height was fixed at one end while a weight was attached to the other end. Actuation was performed by light-induced heating with the set-up described above. Cyclic actuation was investigated in distilled water, whereas lifting of  $\approx 2$  g was performed in air.

The light-controlled gripper was fabricated using a bilayer-structured star-shaped sample (0.18 vol% EG, 10.8 vol% diluted cross-linker solution) attached to a thin rod. To achieve a grasping movement, the actuator was illuminated with 0.44 W cm<sup>-2</sup> using the beamer set-up in air. Releasing of the object was done by immersing the gripper in distilled water ( $T < \text{LCST}$ ).

The electrical gripper was 3D-printed using poly(lactic acid). Silver wires were attached to a PNIPAM-EG hydrogel (0.35 vol% EG, 16.1 vol% diluted cross-linker solution) at the copper foil with conductive silver paste (Acheson 1415). The hydrogel was then fixed at the desired position with superglue. For actuation a voltage of 25 V was applied. The experiment was performed in water.

## Supporting Information

Supporting Information is available from the Wiley Online Library or from the author.

## Acknowledgements

M.H. and L.M.S. contributed equally to this work. The authors thank Dr. Jürgen Carstensen for fruitful discussions. M.H., R.A., and F.S. gratefully acknowledge funding by the German Research Foundation (DFG) through the Research Training Group 2154 "Materials for Brain" (Project P3) and



grant SCHU 3506/4-1. This project has received funding from the Federal Ministry of Education and Research of Germany (BMBF) under the umbrella of the WIR! Initiative "BlueHealthTech" (BHT). L.M.S., A.S.N., X.F., R.A., F.S., and the Humboldtian N.M.P. gratefully acknowledge funding by the European Commission through the GrapheneCore3 881603 Project. B.Z.P. and F.S. acknowledge support by the Kiel Nano Surface and Interface Science (KINSIS).

Open access funding enabled and organized by Projekt DEAL.

## Conflict of Interest

The authors declare no conflict of interest.

## Data Availability Statement

The data that support the findings of this study are available from the corresponding author upon reasonable request.

## Keywords

poly(*N*-isopropylacrylamide), soft actuators, thermoresponsive hydrogels

Received: March 27, 2023

Revised: June 22, 2023

Published online:

- [1] Y. Lee, W. J. Song, J.-Y. Sun, *Mater. Today Phys.* **2020**, *15*, 100258.
- [2] H. Yuk, J. Wu, X. Zhao, *Nat. Rev. Mater.* **2022**, *7*, 935.
- [3] D. Rus, M. T. Tolley, *Nature* **2015**, *521*, 467.
- [4] J. Fang, Y. Zhuang, K. Liu, Z. Chen, Z. Liu, T. Kong, J. Xu, C. Qi, *Adv. Sci.* **2022**, *9*, 2104347.
- [5] X. Xia, C. M. Spadaccini, J. R. Greer, *Nat. Rev. Mater.* **2022**, *7*, 683.
- [6] Y. Li, L. Liu, H. Xu, Z. Cheng, J. Yan, X.-M. Xie, *ACS Appl. Mater. Interfaces* **2022**, *14*, 32541.
- [7] L. Li, J. M. Scheiger, P. A. Levkin, *Adv. Mater.* **2019**, *31*, 1807333.
- [8] P. Techawanitchai, M. Ebara, N. Idota, T.-A. Asoh, A. Kikuchi, T. Aoyagi, *Soft Matter* **2012**, *8*, 2844.
- [9] G. H. Kwon, J. Y. Park, J. Y. Kim, M. L. Frisk, D. J. Beebe, S.-H. Lee, *Small* **2008**, *4*, 2148.
- [10] J. Ko, C. Kim, D. Kim, Y. Song, S. Lee, B. Yeom, J. Huh, S. Han, D. Kang, J.-S. Koh, J. Cho, *Sci. Rob.* **2022**, *7*, eabo6463.
- [11] M. Li, A. Pal, A. Aghakhani, A. Pena-Francesch, M. Sitti, *Nat. Rev. Mater.* **2022**, *7*, 235.
- [12] Y. Ma, M. Hua, S. Wu, Y. Du, X. Pei, X. Zhu, F. Zhou, X. He, *Sci. Adv.* **2020**, *6*, abd2520.
- [13] M. R. Islam, M. L. Oyen, *J. Mater. Res.* **2020**, *12*, 2582.
- [14] S. Poppinga, C. Zollfrank, O. Prucker, J. Rühle, A. Menges, T. Cheng, T. Speck, *Adv. Mater.* **2018**, *30*, 1703653.
- [15] X.-Z. Zhang, X.-D. Xu, S.-X. Cheng, R.-X. Zhuo, *Soft Matter* **2008**, *4*, 385.
- [16] M. Ding, L. Jing, H. Yang, C. E. Machnicki, X. Fu, K. Li, I. Y. Wong, P.-Y. Chen, *Mater. Today Adv.* **2020**, *8*, 100088.
- [17] K. N. Plunkett, X. Zhu, J. S. Moore, D. E. Leckband, *Langmuir* **2006**, *22*, 4259.
- [18] M. Heskins, J. E. Guillet, *J. Macromol. Sci., Chem.* **1968**, *2*, 1441.
- [19] S. Fujishige, K. Kubota, I. Ando, *J. Phys. Chem.* **1989**, *93*, 3311.
- [20] T. Spratte, C. Arndt, I. Wacker, M. Hauck, R. Adelung, R. R. Schröder, F. Schütt, C. Selhuber-Unkel, *Adv. Intell. Syst.* **2022**, *4*, 2100081.
- [21] T. G. Park, A. S. Hoffman, *J. Appl. Polym. Sci.* **1994**, *52*, 85.
- [22] Y. Kaneko, K. Sakai, A. Kikuchi, R. Yoshida, Y. Sakurai, T. Okano, *Macromolecules* **1995**, *28*, 7717.
- [23] L.-W. Xia, R. Xie, X.-J. Ju, W. Wang, Q. Chen, L.-Y. Chu, *Nat. Commun.* **2013**, *4*, 588.
- [24] A. Beck, F. Obst, D. Gruner, A. Voigt, P. J. Mehner, S. Gruenzner, R. Koerbitz, M. H. Shahadha, A. Kutscher, G. Paschew, U. Marschner, A. Richter, *Adv. Mater. Technol.* **2022**, *8*, 2200417.
- [25] Y. Alsaïd, S. Wu, D. Wu, Y. Du, L. Shi, R. Khodambashi, R. Rico, M. Hua, Y. Yan, Y. Zhao, D. Aukes, X. He, *Adv. Mater.* **2021**, *33*, 2008235.
- [26] Y. Pan, Z. Yang, C. Li, S. U. Hassan, H. C. Shum, *Sci. Adv.* **2022**, *8*, eabo1719.
- [27] K. Shi, Z. Liu, Y.-Y. Wei, W. Wang, X.-J. Ju, R. Xie, L.-Y. Chu, *ACS Appl. Mater. Interfaces* **2015**, *7*, 27289.
- [28] X. Qian, Y. Zhao, Y. Alsaïd, X. Wang, M. Hua, T. Galy, H. Gopalakrishna, Y. Yang, J. Cui, N. Liu, M. Marszewski, L. Pilon, H. Jiang, X. He, *Nat. Nanotechnol.* **2019**, *14*, 1048.
- [29] Q. Shi, H. Xia, P. Li, Y.-S. Wang, L. Wang, S.-X. Li, G. Wang, C. Lv, L.-G. Niu, H.-B. Sun, *Adv. Opt. Mater.* **2017**, *5*, 1700442.
- [30] C.-Y. Lo, Y. Zhao, C. Kim, Y. Alsaïd, R. Khodambashi, M. Peet, R. Fisher, H. Marvi, S. Berman, D. Aukes, X. He, *Mater. Today* **2021**, *50*, 35.
- [31] R. Luo, J. Wu, N.-D. Dinh, C.-H. Chen, *Adv. Funct. Mater.* **2015**, *25*, 7272.
- [32] S. I. Rich, R. J. Wood, C. Majidi, *Nat. Electron.* **2018**, *1*, 102.
- [33] C. A. Aubin, B. Gorissen, E. Milana, P. R. Buskohl, N. Lazarus, G. A. Slipher, C. Keplinger, J. Bongard, F. Iida, J. A. Lewis, R. F. Shepherd, *Nature* **2022**, *602*, 393.
- [34] H. Warren, M. in het Panhuis, G. M. Spinks, D. L. Officer, *J. Polym. Sci., Part B: Polym. Phys.* **2018**, *56*, 46.
- [35] C. Yu, Z. Duan, P. Yuan, Y. Li, Y. Su, X. Zhang, Y. Pan, L. L. Dai, R. G. Nuzzo, Y. Huang, H. Jiang, J. A. Rogers, *Adv. Mater.* **2013**, *25*, 1541.
- [36] J. G. Choi, H. Gwac, Y. Jang, C. Richards, H. Warren, G. Spinks, S. J. Kim, *Micromachines* **2021**, *12*, 210.
- [37] C. Arndt, M. Hauck, I. Wacker, B. Zeller-Plumhoff, F. Rasch, M. Taale, A. S. Nia, X. Feng, R. Adelung, R. R. Schröder, F. Schütt, C. Selhuber-Unkel, *Nano Lett.* **2021**, *21*, 3690.
- [38] J. Li, A. Reimers, K. M. Dang, M. G. K. Brunk, J. Drewes, U. M. Hirsch, C. Willems, C. E. H. Schmelzer, T. Groth, A. S. Nia, X. Feng, R. Adelung, W. D. Sacher, F. Schütt, J. K. S. Poon, *Biosens. Bioelectron.* **2023**, *222*, 114942.
- [39] F. Rasch, F. Schütt, L. M. Saure, S. Kaps, J. Strobel, O. Polonskyi, A. S. Nia, M. R. Lohe, Y. K. Mishra, F. Faupel, L. Kienle, X. Feng, R. Adelung, *ACS Appl. Mater. Interfaces* **2019**, *11*, 44652.
- [40] A. Kozbial, Z. Li, C. Conaway, R. McGinley, S. Dhingra, V. Vahdat, F. Zhou, B. D'Urso, H. Liu, L. Li, *Langmuir* **2014**, *30*, 8598.
- [41] V. P. Gilcreest, W. M. Carroll, Y. A. Rochev, I. Blute, K. A. Dawson, A. V. Gorelov, *Langmuir* **2004**, *20*, 10138.
- [42] B. Isik, M. Kis, *J. Appl. Polym. Sci.* **2004**, *94*, 1526.
- [43] A. Jastram, T. Lindner, C. Luebbert, G. Sadowski, U. Kragl, *Polymers* **2021**, *13*, 1834.
- [44] F. Schütt, F. Rasch, N. Deka, A. Reimers, L. M. Saure, S. Kaps, J. Rank, J. Carstensen, Y. Kumar Mishra, D. Misseroni, A. Romani Vázquez, M. R. Lohe, A. Shaygan Nia, N. M. Pugno, X. Feng, R. Adelung, *Mater. Today* **2021**, *48*, 7.
- [45] D. Kim, H. Kim, E. Lee, K. S. Jin, J. Yoon, *Chem. Mater.* **2016**, *28*, 8807.
- [46] T. S. Shim, S.-H. Kim, C.-J. Heo, H. C. Jeon, S.-M. Yang, *Angew. Chem., Int. Ed.* **2012**, *51*, 1420.
- [47] C. Yao, Z. Liu, C. Yang, W. Wang, X.-J. Ju, R. Xie, L.-Y. Chu, *Adv. Funct. Mater.* **2015**, *25*, 2980.
- [48] W. J. Zheng, N. An, J. H. Yang, J. Zhou, Y. M. Chen, *ACS Appl. Mater. Interfaces* **2015**, *7*, 1758.
- [49] Y. Yamamoto, K. Kanao, T. Arie, S. Akita, K. Takei, *ACS Appl. Mater. Interfaces* **2015**, *7*, 11002.
- [50] D. Kim, H. S. Lee, J. Yoon, *Sci. Rep.* **2016**, *6*, 20921.
- [51] Y. Jian, B. Wu, X. Yang, Y. Peng, D. Zhang, Y. Yang, H. Qiu, H. Lu, J. Zhang, T. Chen, *Supramol. Mater.* **2022**, *1*, 100002.

- [52] H. Warren, D. J. Shepherd, M. in het Panhuis, D. L. Officer, G. M. Spinks, *Sens. Actuators, A* **2020**, *301*, 111784.
- [53] B. S. Forney, C. A. Guymon, *Macromol. Rapid Commun.* **2011**, *32*, 765.
- [54] Y. K. Mishra, S. Kaps, A. Schuchardt, I. Paulowicz, X. Jin, D. Gedamu, S. Freitag, M. Claus, S. Wille, A. Kovalev, S. N. Gorb, R. Adelung, *Part. Syst. Charact.* **2013**, *30*, 775.
- [55] Y. K. Mishra, G. Modi, V. Cretu, V. Postica, O. Lupan, T. Reimer, I. Paulowicz, V. Hrkac, W. Benecke, L. Kienle, R. Adelung, *ACS Appl. Mater. Interfaces* **2015**, *7*, 14303.
- [56] J. Moosmann, A. Ershov, V. Weinhardt, T. Baumbach, M. S. Prasad, C. LaBonne, X. Xiao, J. Kashef, R. Hofmann, *Nat. Protoc.* **2014**, *9*, 294.
- [57] W. van Aarle, W. J. Palenstijn, J. de Beenhouwer, T. Altantzis, S. Bals, K. J. Batenburg, J. Sijbers, *Ultramicroscopy* **2015**, *157*, 35.
- [58] W. van Aarle, W. J. Palenstijn, J. Cant, E. Janssens, F. Bleichrodt, A. Dabrovolski, J. de Beenhouwer, K. Joost Batenburg, J. Sijbers, *Opt. Express* **2016**, *24*, 25129.
- [59] S. Bruns, S. L. S. Stipp, H. O. Sørensen, *Adv. Water Resour.* **2017**, *105*, 96.
- [60] I. Arganda-Carreras, V. Kaynig, C. Rueden, K. W. Eliceiri, J. Schindelin, A. Cardona, H. S. Seung, *Bioinformatics* **2017**, *33*, 2424.
- [61] J. Schindelin, I. Arganda-Carreras, E. Frise, V. Kaynig, M. Longair, T. Pietzsch, S. Preibisch, C. Rueden, S. Saalfeld, B. Schmid, J.-Y. Tinevez, D. J. White, V. Hartenstein, K. Eliceiri, P. Tomancak, A. Cardona, *Nat. Methods* **2012**, *9*, 676.